Solar Energy Materials & Solar Cells 233 (2021) 111386

Contents lists available at ScienceDirect

Solar Energy Materials and Solar Cells

journal homepage: www.elsevier.com/locate/solmat

# Atomic-layer-deposited Al-doped zinc oxide as a passivating conductive contacting layer for $n^+$-doped surfaces in silicon solar cells

Bart Macco [a,*], Bas W.H. van de Loo [a], Marc Dielen [a], Dennis G.J.A. Loeffen [a], Bart B. van Pelt [a], Nga Phung [a], Jimmy Melskens [a,b], Marcel A. Verheijen [a], Wilhelmus M.M. Kessels [a]

[a] Department of Applied Physics, Eindhoven University of Technology, P.O. Box 513, 5600 MB, Eindhoven, the Netherlands
[b] TNO Energy Transition, Solar Energy, Westerduinweg 3, 1755 ZG Petten, the Netherlands

ARTICLE INFO

*Keywords:*
Passivating contact
Atomic layer deposition
Surface passivation
Crystalline silicon solar cells
Transparent conductive oxide

ABSTRACT

Stacks consisting of an ultrathin $SiO_2$ coated with atomic-layer deposited (ALD) zinc oxide (ZnO) and aluminum oxide ($Al_2O_3$) have been shown to yield state-of-the-art passivation of *n*-type crystalline silicon surfaces. The distinguishing aspect of this novel passivation stack is the very conductive nature of the passivating ZnO layer. In this work, it is demonstrated that such a stack can provide additional functionalities relevant for silicon solar cells. Specifically, it is shown that the conductive and transparent stacks can passivate textured and $n^+$-diffused silicon surfaces and that they can form an Ohmic contact to $n^+$ -diffused surfaces with a low contact resistivity, provided the ZnO is Al-doped. The $Al_2O_3$ capping layer has previously been shown to be crucial in the passivation mechanism by preventing the effusion of hydrogen during annealing. Here, it is demonstrated to enable a significant improvement in both the transparency and lateral conductivity of the ZnO upon annealing as well, up to a level typically only attainable by In-based transparent conductive oxides. It is furthermore shown that the passivation of the stacks is thermally stable up to 500–600 °C, depending on the preparation method for the interfacial $SiO_2$. Together, these properties make the presented stack an interesting building block for crystalline silicon solar cells, with possibilities for integration as passivating front contact in Passivated Emitter and Rear Cell (PERC)-like solar cells, e.g. as bottom cell top contact in silicon-perovskite tandem cells, as well as a conductive hydrogenation source for poly-Si passivating contacts.

## 1. Introduction

In the field of crystalline silicon (*c*-Si) solar cells, engineering and tailoring of the contacts is becoming progressively important as the conversion efficiencies creep more and more towards the efficiency limit, which is set at 29.43% for single-junction *c*-Si solar cells [1]. The contacting scheme should simultaneously exhibit a combination of functionalities, which together dictate the efficiency potential. Firstly, the contacting scheme should allow for the extraction of majority charge carriers (either electrons or holes) with low Ohmic losses, i.e. the contact resistivity $\rho_c$ should be low. At the same time, recombination of minority carriers should be suppressed, thus enabling a low recombination parameter $J_0$ [2–7]. Together, these two parameters define the charge-carrier *selectivity* of the contacting scheme. Besides selectivity, which relates to the collection and loss of carriers at the contacts, the contacting scheme should also maximize the photogeneration of carriers by providing proper antireflection and exhibiting low parasitic optical losses, as well as providing sufficient lateral conductivity towards the metal contacting grid in order to mitigate Ohmic losses. The goal of simultaneously satisfying these requirements to the maximum extent, preferably using low-complexity, robust and inexpensive processes, is the main challenge for solar cell contact design and has become a major driver for process and material research and development in this field [2].

The wide variety of contacting approaches and designs that exists in research and production can be classified in two major categories, i.e. *homojunctions* and *heterojunctions*, where the latter is also often referred to as *passivating contacts*. The ZnO-based contacts introduced in this work have potential applications in both categories, and as such, the main aspects, perks and challenges for both categories are briefly summarized here. In homojunction designs, the carrier selectivity arises from highly $n^+$ or $p^+$ doped silicon regions, which additionally provide lateral conductivity of the charge carriers to the metal contacts. Surface passivation layers – typically silicon nitride ($SiN_x$) or aluminum oxide

* Corresponding author.
*E-mail address:* b.macco@tue.nl (B. Macco).

https://doi.org/10.1016/j.solmat.2021.111386
Received 9 February 2021; Received in revised form 21 July 2021; Accepted 6 September 2021
Available online 15 September 2021

($Al_2O_3$) capped by $SiN_x$ – passivate the regions of the doped *c*-Si surface which are not contacted by the metal and improve the optical incoupling in the cell [8,9]. For such homojunctions, a large part of the optimization challenge lies in the doping profile and firing-through contacting. Underneath the metal contacts, the doping profile should be sufficiently strong to shield the minority carriers from the recombination-active Si-metal interface and to enable a low *c*-Si-metal contact resistivity [6]. On the other hand, a high doping level of the *c*-Si inevitably leads to Auger recombination losses, increasing $J_0$ and consequently limiting the open-circuit voltage ($V_{oc}$) of the solar cell [10]. For the passivated regions in between the metal contacts, the requirements for the doped region are markedly different. Here, shielding of the minority carrier from the *c*-Si surface is much less critical, as the surface is passivated [11]. The main criterion is to achieve lateral conductivity towards the metal grid without inducing excessive Auger recombination and optical losses in the form of free-carrier absorption (FCA) and reflection. These considerations typically translate to a more lowly-doped optimal doping profile. Hence, the contacted and passivated regions of e.g. the front side of a PERC (passivated emitter and rear contact) cell differ in their optimal diffusion profile. Practically speaking, this discrepancy forces manufacturers to optimize a single, uniform diffusion profile that meets these demands to the maximum extent, or to apply locally a different doping profile underneath the metal contacts. The latter is for example done using laser doping from the phosphosilicate glass (PSG). This improves cell efficiency but also adds to the processing complexity [12].

For heterojunction or passivating contact structures, the design criteria and boundary conditions are markedly different. These contact structures are typically formed using a stack of layers: (1) A passivation layer such as amorphous silicon or a hydrogenated tunnel layer of $SiO_2$ [13–18]. (2) A carrier-selective material which induces selectivity through (a combination of) high doping (e.g. doped amorphous or polycrystalline silicon sometimes alloyed with O or C) [19–21], work function differences (e.g. the hole-selective contacts $MoO_x$, $WO_x$ and $VO_x$) [22–30] or suitable band alignment and offsets (e.g. the electron-selective contact $TiO_x$) [31–33]. (3) A transparent conductive oxide (TCO) to provide lateral conductivity and antireflection. Typical materials include indium oxide ($In_2O_3$) and zinc oxide (ZnO), *n*-type doped with elements such as Sn, Al or H. (4) Screen-printed local silver contacts (non-firing through).

The main perks of the heterojunction approach are the full-area passivation without direct *c*-Si-metal contact and the absence of a highly doped *c*-Si region, resulting in very low recombination losses and hence superior $V_{oc}$ values. The more pressing challenges for these contacts lie in simultaneously achieving high selectivity, transparency and lateral conductivity. Specifically, doped amorphous and polycrystalline silicon can be very carrier-selective (i.e. low $J_0$ and low $\rho_c$), but their low band gaps lead to optical losses that limit the short-circuit current density $J_{sc}$ when applied at the front side, or the bifaciality when applied at the rear side of the solar cell [2,34]. On the other hand, metal oxides such as $MoO_x$ and $TiO_x$ can be very transparent due to their high band gap, but these typically yield less stable selectivity and relatively high $\rho_c$ values [2,29,35,36]. Optical transparency is also a challenge for the TCO layers, as there is an inevitable trade-off between conductivity and optical transparency: In order to achieve a sufficiently low sheet resistance (typically less than 100 Ω/sq.), the TCO is degenerately *n*-type doped to a carrier density $N_e$ of a few times $10^{20}$ $cm^{-3}$. This high doping however brings the plasma frequency $\omega_p$ of the TCO into the N(IR) region, resulting in optical free-carrier (or Drude) losses through absorption and reflection [34]. Hence, there is an active field of research to improve the mobility of the TCOs, such that a high conductivity can be reached while keeping Drude losses at bay [37–43]. Finally, since this work deals on ZnO as contacting material, it is instructive to point out that ZnO has already been explored in various works as an electron-selective contact and efficiencies exceeding 21% have been obtained [44–46]. In those works, dedicated amorphous silicon passivation layers are used since the ZnO layer does not provide surface passivation. In addition, the inclusion of an ultrathin LiF layer in between the ZnO and Al metallization is commonly used to improve the contact further [44,45].

Within this context, it is interesting to consider stacks of ALD ZnO and $Al_2O_3$. Recently we have shown that these stacks -similarly as $Al_2O_3$ and $SiN_x$-can serve as an excellent hydrogenation source for $SiO_2$/poly-Si(n) contacts upon annealing at 450–500 °C [47,48]. In addition, we have shown that ZnO/$Al_2O_3$ stacks can provide state-of-the-art passivation on *n*-type *c*-Si directly, as witnessed by implied $V_{oc}$ levels of 728 mV [49]. In this prior work of van de Loo et al., the passivation principle of this stack has been shown to rely on a few key aspects. Firstly, preparing a high-quality $SiO_2$ interlayer prior to ALD of ZnO is required, as ALD ZnO does not naturally form a high-quality $SiO_2$ interface with *c*-Si. Secondly, during an activation anneal at 400–450 °C, the ALD $Al_2O_3$ capping layer prevents effusion of hydrogen, such that the hydrogen can passivate interfacial defects in the $SiO_2$. The passivation level is relatively insensitive to ZnO film thickness, as similar passivation was achieved for 13 and 75 nm-thick films. Moreover, the *field-effect* passivation of the stack can be improved by doping of the ZnO, which results in a lowering of the work function and hence increases the downward band bending at the *c*-Si surface. Finally, it is good to note the $Al_2O_3$ layer is *sacrificial*, i.e. it can be removed selectively and wet-chemically after the post-deposition anneal without impairing the surface passivation [50].

In this work, it is demonstrated that in addition to providing surface passivation, this novel passivation scheme can also serve as a lateral transport, antireflection and contacting layer to $n^+$-diffused *c*-Si surfaces, such that it has the potential to enable a hybrid approach between homo- and heterojunction contacts where a highly-doped Si surface is contacted by a passivating TCO. Several important aspects for such use of these stacks are explored and demonstrated. Specifically, it is shown that the stacks can passivate both textured and $n^{+}$-diffused silicon and that ALD ZnO on a thin $SiO_2$ layer can form an Ohmic contact to such $n^{+}$-diffused surfaces with a low contact resistivity. Doping of both the *c*-Si and the ZnO:Al is shown to aid in reducing the contact resistivity considerably. It is furthermore shown that the interfacial $SiO_2$ can be prepared by various preparation methods and that the stack is thermally stable up to 550–600 °C. From electron microscopy studies, it is shown that this upper limit of thermal stability is related to degradation of the interfacial $SiO_2$, as well as to the appearance of voids in the ZnO at high annealing temperatures. Furthermore, the presence of the $Al_2O_3$ capping layer during annealing is shown not only to be crucial for achieving surface passivation, but also for significantly improving the optoelectronic properties of the doped ZnO. Specifically, the charge carrier mobility is enhanced such that the transparency and conductivity reach levels typical to those of In-based TCOs. Finally, opportunities and potential benefits for the application of the stack as front contact in PERC-type solar cells and poly-Si(n) passivating contacts are outlined.

## 2. Experimental section

In this study four different sample structures were used, schematically shown in Fig. 1. Type A and B samples are symmetrical lifetime test structures that have a stack of $SiO_x$/ZnO(:Al)/$Al_2O_3$ on both sides of the substrate. Type A samples feature mirror-polished 285 μm thick *n*-type floatzone (FZ) wafers with a resistivity of 3 Ωcm as substrate. These type A samples were used to compare various $SiO_x$ interlayers, prepared by UV/$O_3$, nitric acid oxidation step (NAOS) [51], low-temperature dry oxidation at 610 °C (LTO) or Radio Corporation of America (RCA) cleans. Type B samples were used to investigate the passivation performance of the stack on textured and $n^+$-diffused Si surfaces. These type B samples were prepared on KOH-textured 185 μm-thick *n*-type Czochralski (CZ) wafers with a base resistivity of 3 Ωcm. Select samples feature a $n^+$-diffused surface prepared by $POCl_3$ diffusion in a tube furnace. Type C samples are symmetrical samples featuring a stack of UV/$O_3$ $SiO_x$/ZnO(:Al)/Ag on $n^+$-diffused surfaces and were used to determine the contact resistivity. The doping level of both the $n^+$ Si and

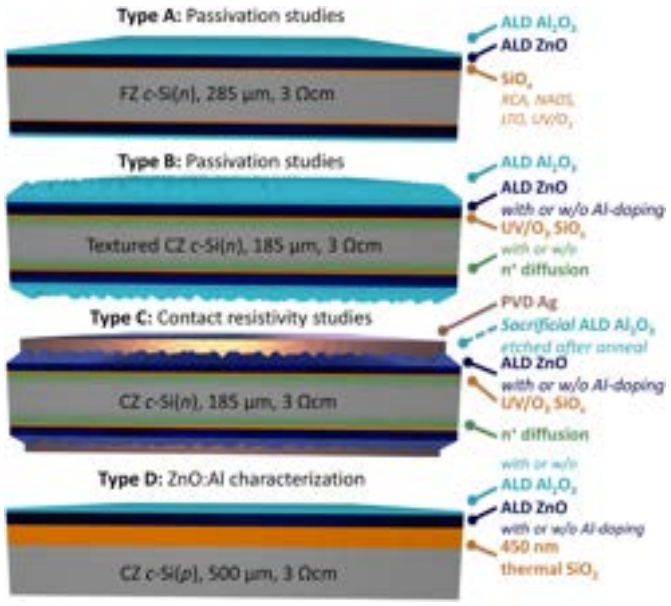


**Fig. 1.** Schematic illustrations of the four samples structures studied in this work. The figures are not to scale.

the ZnO:Al were varied to investigate their effect on the contact resistivity. These samples received the same 30 nm $Al_2O_3$ capping layer and subsequent anneal treatments as the type A and B samples. However, to enable contacting by Ag the $Al_2O_3$ capping layer was subsequently wet-etched selectively from the ZnO(:Al). This selective wet etch was performed in a 0.1 M $Na_2CO_3$ solution at 60 °C, of which the pH was controlled to 11.8 by the addition of KOH. Subsequently, 300 nm of blanket Ag was deposited on both sides of the wafer by e-beam evaporation. For comparison, select samples featured a $SiO_2$/poly-Si(n) passivating contact prepared by LPCVD instead of an $n^+$-diffused Si surface. These type C samples were cut into ~0.7x0.7 $cm^2$ samples after deposition in order to define small samples with little spreading resistance and at the same time avoid possible shunts by ALD ZnO that typically has a few millimeters of wrap-around deposition on our ALD reactor. Type D samples are single-sided samples that feature a 450 nm thermal $SiO_2$ layer, followed by ALD of intrinsic or Al-doped ZnO (ZnO:Al), with or without a 30 nm ALD $Al_2O_3$ capping layer. These samples were used for the determination of the optoelectronic properties of the ALD ZnO(:Al) by spectroscopic ellipsometry (SE) and Hall measurements, and the effect of annealing thereon. The 450 nm thermal $SiO_2$ layer serves as an optical spacer to enhance the sensitivity of the spectroscopic ellipsometry (SE) measurement as well as an electrical insulation layer to confine the flow of current purely to the ZnO film during the Hall measurements. Note that for these samples the probes for the Hall measurement readily puncture through the ALD $Al_2O_3$ capping layer, enabling contacting of the ALD ZnO(:Al) without removal of the $Al_2O_3$ capping layer.

Type A wafers received RCA 1 and 2 cleans, which leaves an RCA interfacial oxide. This RCA oxide was either left on or stripped by dipping in 1% hydrofluoric acid (HF) for 1 min prior to oxidation by the alternative methods ($UV/O_3$, NAOS or LTO). NAOS oxidation was performed by dipping in a 68 wt % $HNO_3$ solution for 10 min at room temperature. Type B and C wafers received a 1% HF dip for 1 min, followed by 30 min $UV/O_3$ oxidation. $UV/O_3$ oxidation was performed at room temperature in a Novascan PSD Series UV Ozone Cleaner.

ZnO:Al and $Al_2O_3$ thin films were prepared by thermal ALD in an Oxford Instruments OpAL reactor. The table and wall temperatures were kept at 200 °C and 180 °C for all ALD runs, respectively. For ZnO and $Al_2O_3$ depositions, diethylzinc (DEZ) and trimethylaluminum (TMA) were used as precursors, respectively, and $H_2O$ as oxygen source. For Al-doping of the ZnO, dimethylaluminumisopropoxide (DMAI) was used as an efficient doping precursor [52]. Doping was introduced in a supercycle fashion, in which an integer $n$ ZnO ALD cycles was alternated by one DMAI cycle [53]. The cycle ratio $n$ was used to accurately control the Al doping level [3,54]. Note that our supercycle recipes were designed such that one supercycle consists of $n/2$ ZnO cycles, one Al dopant cycle, followed by $n/2$ ZnO cycles. This ensures a more homogeneous distribution of the dopant planes throughout the thickness of the film, especially when only few dopant cycles are introduced in the film. In addition, the final cycle would otherwise be a dopant step. Cycle ratios $n$ of 96, 48, 24 and 16 were used, and from X-ray photoelectron (XPS) the resulting Al concentration in at. % was estimated to be 0.4, 0.8, 1.7 and 2.6%, respectively. For the passivation studies and contact resistivity measurements a ZnO(:Al) thickness of 20 nm was used, since our previous work showed that equally good passivation can be obtained for films as thin as 13 nm as for the device-relevant thickness of approximately 75 nm [49]. For type D samples the ZnO(:Al) films had a thickness of 75–85 nm since the optoelectronic quality of TCOs typically increases with film thickness. The sacrificial $Al_2O_3$ films have a thickness of 30 nm for all sample types. Post-deposition forming gas anneals (FGA, 10/90 $H_2/N_2$) at approximately 700 mbar were performed in a Jipelec rapid thermal anneal (RTA) furnace. For type D samples, post-deposition anneals up to 500 °C were performed on a hot plate in ambient, whereas higher temperature annealing was performed in the aforementioned RTA system in forming gas. It was verified using a type D sample with an $Al_2O_3$ capping layer that both annealing approaches lead to very similar electrical properties.

The passivation quality, expressed as either the implied open-circuit voltage ($iV_{oc}$) or the recombination current density ($J_0$) was evaluated using a Sinton WCT-120TS lifetime tester. The optical factor for the lifetime measurement was determined from optical simulations using the PVLighthouse OPAL2 calculator, using measured optical constants of the layers as input [55]. The $J_0$ values were extracted for injection levels between 1 and 5 x $10^{15}$ $cm^{-3}$ using the Kane & Swanson method [56]. The model of Richter *et al.* was used for the bulk lifetime [10]. The thickness of the $SiO_x$ interlayers was evaluated from SE using fixed tabulated optical constants (NTVE_JAW of J.A. Woollam). Note that the oxide thickness determined from SE can slightly deviate from the real oxide thickness due to the assumption of a certain fixed refractive index [15]. SE was also used for determination of the optical constants of the ALD ZnO(:Al). The optical constants were modelled by a Tauc-Lorentz and a Drude oscillator [57]. The absorption coefficient α was calculated from the optical constants using the relation $\alpha = \frac{4\pi k}{\lambda}$.

Upper bounds for specific contact resistivities were obtained through top-down measurements on symmetric type C samples, after removal of the sacrificial $Al_2O_3$ capping layer by wet-etching and subsequent capping with evaporated Ag. To enable four-terminal measurements while ensuring that the driven current distribution is uniform, top-down measurements are performed using interdigitated contacts on both sides of the sample. More information on this measurement setup can be found in the supplementary information.

In order to study the sample structure and interfaces, select Type C samples were investigated by TEM (JEOL ARM 200 probe corrected TEM, operated at 200 kV) in cross section using Focused Ion Beam made lamella. In addition, the distribution of Al dopants was visualized using energy-dispersive X-ray spectroscopy (EDX).

## 3. Results and discussion

In order to study the passivation performance of the various $SiO_x$ types, symmetrical lifetime samples of type A were prepared. The $SiO_x$ thickness was determined by ellipsometry, prior to ALD of the ZnO/$Al_2O_3$ stack. After ALD, the samples were subjected to a 30-min FGA at 450 °C and their passivation quality was measured. Fig. 2 shows the thicknesses and resulting passivation quality for the various $SiO_x$ types

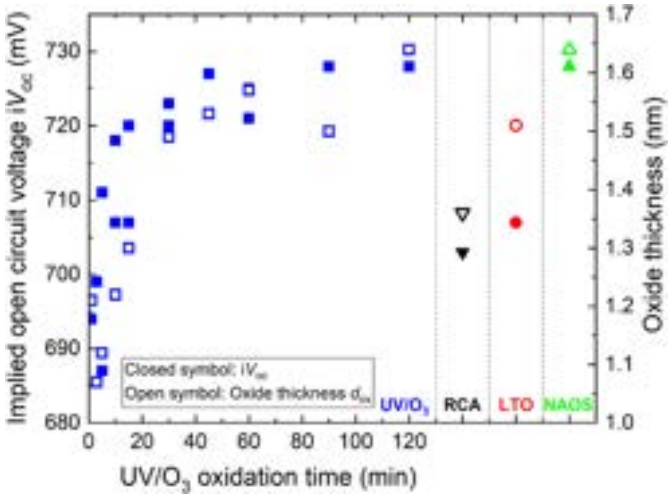


**Fig. 2.** (Open symbols) $SiO_x$ thickness as determined from ellipsometry, prior to ALD ZnO deposition. (Closed symbols) $iV_{oc}$ values for $SiO_x$/ZnO/$Al_2O_3$ stacks on type A samples, after a 30 min FGA at 450 °C. The ZnO and $Al_2O_3$ layers were 20 and 30 nm thick, respectively. The $SiO_x$ layers were prepared by UV/$O_3$ oxidation, Radio Corporation of America cleans (RCA), low-temperature oxidation (LTO) or a nitric acid oxidation step (NAOS).

studied. For the UV/$O_3$ treatment, the oxide thickness initially increases rapidly with oxidation time, followed by a soft saturation to ~1.6 nm. The passivation quality, expressed in terms of $iV_{oc}$, shows a similar trend, saturating at an excellent value close to 730 mV. The RCA and LTO oxides exhibit both a lower oxide thickness and passivation quality, whereas the NAOS oxide thickness and passivation quality are very similar to the UV/$O_3$ oxide. These results suggest that the resulting passivation quality is mostly dependent on the thickness of the interfacial oxide rather than on the preparation method.

When looking at stepwise annealing at progressively increasing temperatures, it becomes apparent that the activation temperature, optimal annealing temperature and the thermal stability of the passivation quality vary with the oxide preparation method, as shown in Fig. 3. Specifically, the passivation provided by the UV/$O_3$ oxide is activated at relatively lower annealing temperatures and peaks at 450–500 °C, while also being the least thermally stable. The wet-chemical RCA and NAOS

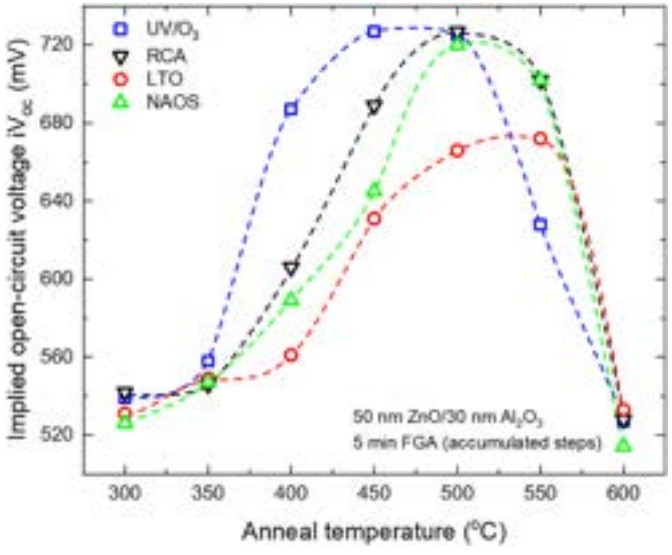


**Fig. 3.** $iV_{oc}$ for $SiO_x$/ZnO/$Al_2O_3$ stacks on type A samples, where the interfacial oxide was prepared by either 30 min UV/$O_3$, RCA, LTO or NAOS. Consecutive annealing steps were performed for 5 min in forming gas ambient.

oxides show the best passivation after annealing at 500 °C, reaching a level similar to that of the UV/$O_3$ oxide. The passivation of the LTO oxide reaches its best value at an even higher annealing temperature of 550 °C, though it does not reach the values achieved by the oxides prepared at room temperature. A similar trend was observed in a comparative study of the passivation of tunnel oxides in poly-Si passivating contacts [58]. Also for such contacts, thermally-grown oxides tend to have a higher optimal annealing temperature, albeit that significantly higher temperatures of 850–1050 °C were studied. Finally, for all oxide types the passivation is effectively lost after forming gas annealing at 600 °C.

This loss of passivation is most likely related to roughening of the Si/$SiO_2$/ZnO interface, as will be discussed later on in this work in the section on TEM imaging of the contact structure. Another plausible contributor to the loss of passivation is effusion of hydrogen, as thermal effusion measurements in our previous work on the passivation by ZnO/$Al_2O_3$ stacks indeed showed the effusion of $H_2$ at temperatures above 400–450 °C and even effusion of $H_2O$ at temperatures exceeding approximately 600 °C [49]. The loss of hydrogen can however not be the sole mechanism, as can be inferred from the fact that $SiO_2$/poly-Si/ALD $Al_2O_3$ contacts, examined in our previous work, are thermally stable up to temperatures 600 °C for identical ALD $Al_2O_3$ thickness and FGA ambient [48]. Moreover, if effusion of hydrogen from the stack was the main cause for the loss of passivation, the different onset temperatures at which the passivation starts to decrease that is observed for the different interfacial oxides would not be expected, provided the passivation level of the various oxides reacts similarly to dehydrogenation. Finally, it has been shown in studies on poly-Si(n)/ZnO:Al structures that ZnO can reduce to metallic Zn at temperatures exceeding 600 °C, especially in the presence of hydrogen, and that this Zn can moreover diffuse into the silicon forming recombination centers [59,60]. Although the loss of passivation in this work is observed at somewhat lower temperatures, such a mechanism cannot be excluded.

It was verified that these stacks are not compatible with a high-temperature firing step commonly employed for the metallization in homojunction and poly-Si passivating contact solar cells. This was done by placing a type A sample with a UV/$O_3$ oxide on an industrial firing belt with a peak temperature of 720 °C, resulting in a poor $iV_{oc}$ of 626 mV. Although the stacks are thus not firing-stable, it should be noted that their thermal stability is still significantly higher in comparison to amorphous silicon [61–63] and most oxide-based contacts [64,65], which can potentially enable the use of higher-temperature metal pastes with an improved line conductivity.

### 3.1. Passivation of textured and $n^+$-diffused c-Si surfaces

In previous work, the $SiO_2$/ZnO/$Al_2O_3$ stack has been shown to yield good passivation of mirror-polished and undiffused *n*-type Si surfaces [49]. Here it is demonstrated that this stack is also capable of passivating a variety of surfaces commonly found in Si solar cell structures. Specifically, the compatibility of the stack with textured surfaces and $n^+$-diffused surfaces is demonstrated, as well as its ability to passivate the front surface of PERC half fabricate cells. For type B samples without an $n^+$-diffusion, an $iV_{oc}$ of 728 mV is reached on both mirror-polished and textured surfaces (not shown), which indicates a high level of compatibility with textured surfaces. Fig. 4 shows a comparison of the passivation performance of our ZnO-based stacks on $n^+$-doped -surfaces on a variety of emitter sheet resistances. Specifically, the dataset includes data on both planar and textured surfaces as well as for intrinsic and Al-doped ZnO. Two datapoints were acquired on PERC-type half-fabricates, where the front surface stack is identical to type B samples and the rear surface consists of a proprietary passivation stack. For these samples, the $J_0$ of the front ZnO-based passivation stack was determined by subtraction of the known rear $J_0$ from the total $J_0$. For reference, literature values of commonly-used materials for the passivation of such surfaces have been added.

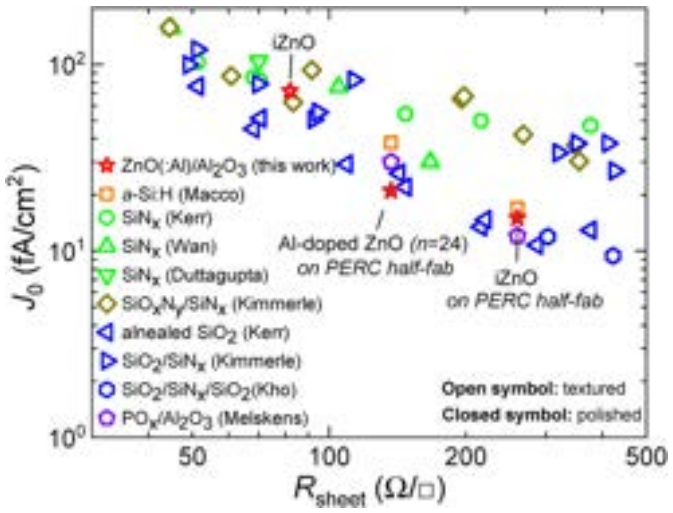


**Fig. 4.** Comparison of the passivation quality of various passivation schemes on textured *c*-Si surfaces with varying levels of $n^+$-doping, resulting in a range of sheet resistances. The graph includes data from this work on $SiO_2$/ALD ZnO(:Al)/$Al_2O_3$ stacks and a selection of other common passivation schemes for the passivation of $n^+$-doped Si reported in the literature [18,66–71]. The $SiO_2$ layer underneath the ALD ZnO(:Al)/$Al_2O_3$ stacks was prepared by a 30 min UV/$O_3$ treatment and the stack was subjected to a forming gas anneal at 450 °C for 5 min. The corresponding i$V_{oc}$ values for the samples from this work are (left to right) 680, 689 and 699 mV.

As can be seen, generally the $J_0$ increases for lower sheet resistances (i.e. stronger $n^+$-doping). This is attributed to enhanced Auger recombination and can in addition stem from the introduction of defects such as inactive P atoms or P precipitates. Promisingly, the passivation performance of the ZnO-based stacks is in line with the performance of conventional passivation schemes. In addition, the results on the PERC half-fabricates demonstrate that also good performance can be achieved on industrially-relevant substrates. It should however be noted that a one-to-one comparison cannot be made since these results were obtained on chemically-polished surfaces, whereas the other datapoints in the plot are all on textured *c*-Si. Nevertheless, these results clearly demonstrate the ability of ZnO(:Al)-based stacks to provide passivation to textured as well as $n^+$-diffused *c*-Si surfaces.

### 3.2. Contacting of n-type Si surfaces by $SiO_2$/ZnO(:Al) stacks

Next, the electrical contacting behavior of the conductive ZnO on *c*-Si was explored. The effect of the doping level of both the *c*-Si($n^+$) and the ZnO:Al on the contact resistivity was investigated, as well as the influence of the annealing treatment used to activate the passivation. To this end, symmetrical Type C samples (see Fig. 1) were used for measuring the contact resistivity. For reference, the contact resistivity to a $SiO_2$/poly-Si($n^+$) passivating contact prepared by LPCVD was also determined.

As can be seen in Fig. 5, doping of both the c-Si($n^+$) and the ZnO:Al is highly effective in reducing the contact resistivity. For undoped ZnO samples, high contact resistivity values in excess of 1 Ωcm$^2$ are obtained on a 260 Ω/sq $n^+$ -diffused surface. For a surface with a stronger 130 Ω/sq $n^+$-diffusion, lower contact resistivity values around 500 mΩcm$^2$ are obtained, which is however still too high for efficient device operation. For all surface types, Al-doping of the ZnO:Al enables a strong reduction in contact resistivity with values below 20 mΩcm$^2$ obtained for both the Al-doped ZnO samples on the 130 Ω/sq $n^+$-diffused surface. As such, it appears that doping of the *c*-Si wafer and ZnO is crucial for obtaining a device-relevant contact quality. Similarly as for $n^+$-diffused surfaces, also on poly-Si(*n*) surfaces Al-doping of the ZnO is prerequisite for achieving low contact resistivity values.

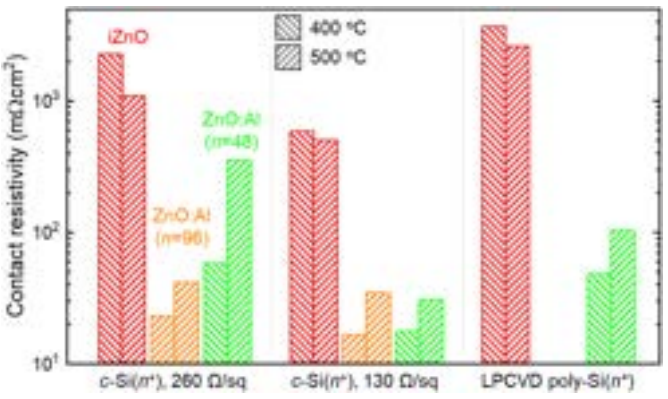


**Fig. 5.** Contact resistivity values for type C samples featuring a 130 or 260 Ω/sq $n^+$-diffusion and with an area of approximately 0.5 cm$^2$. For reference, also the contact resistivity of the stack to a $SiO_2$/poly-Si($n^+$) contact was determined. The substrates featured an $SiO_2$ layer grown by 30 min of UV/$O_3$. Measurements were performed after 5 min of annealing at either 400 or 500 °C.

Interestingly, it appears that lightly-doped ($n$=96) ZnO:Al can outperform more highly-doped ($n$=48) ZnO:Al in terms of contact resistivity. Although the precise mechanism is currently not known, this is reminiscent of results we previously obtained using exactly the same ALD ZnO:Al as TCO on a-Si:H layers in rear-emitter SHJ solar cells [72]. In this work of Niemelä *et al.*, it was observed that the cell series resistance increased strongly for more highly-doped ZnO:Al, which was attributed to a barrier induced by the presence of $Al_2O_3$ at the Si-TCO interface. Specifically, since ALD ZnO tends to grow in islands during the nucleation phase, the substrate surface can experience Al-dopant cycles before the islands have coalesced [54]. This effect is more severe for lower cycle ratios *n*, since less ZnO cycles are performed prior to the first $Al_2O_3$ cycle. It should however be noted that this can in principle be circumvented by the introduction of additional ZnO cycles prior to the ZnO:Al supercycle recipe.

As for the effect of annealing, an opposite trend is observed for the intrinsic and Al-doped ZnO samples: whereas the contact resistivity of the undoped ZnO samples consistently improves further upon annealing at 500 °C, the contact for Al-doped ZnO samples starts to degrade. Although the precise mechanism is not currently known, one possible mechanism is related to diffusion of the Al dopants towards the interface. Accumulation of Al at the interface has previously been found to occur in poly-Si(*n*)/ZnO:Al junctions prepared by solid phase crystallization of a-Si:H(*n*) [59]. The TEM investigations presented in the next section will show that there are hints of Al diffusion in our samples as well. It is also good to note that in a similar study on sputtered ZnO:Al on poly-Si(n) passivating contacts, it was found that the contact resistivity increased strongly at an annealing temperature of 400 °C, which was attributed to the formation of 2–3 nm of $SiO_x$ at the TCO/poly-Si interface [73]. As TEM images will point out in the next section, in our case the interfacial oxide is only 1.1 nm after annealing at 400 °C but thickens upon annealing at 600 °C. Therefore it is well conceivable that this oxide contributes to the contact resistivity of especially the Al-doped films annealed at 500 °C.

### 3.3. Electron microscopy study of the $SiO_2$/ZnO:Al/Ag contact

In order to get insights into the structural properties as well as dopant distribution within the ZnO:Al film, a cross-sectional TEM study of two samples was carried out. Specifically, the sample in Fig. 5 corresponding to the ZnO:Al ($n$=48) layer on the 260 Ω/sq textured $n^+$ surface was used. The sample was either annealed at 400 or 600 °C prior to FIB preparation. These temperatures were chosen since 400 °C is known to yield good surface passivation, whereas at 600 °C this passivation is effectively lost.

In Fig. 6 a selection of TEM images is displayed, obtained from the sample annealed at 400 °C. The Bright Field (BF) TEM figures a) and b) clearly show the conformal coating of the valley of the random-pyramid texture by the ALD ZnO:Al, as well as the presence of the UV/$O_3$ interfacial silicon oxide. The interfacial oxide appears conformal and intact, in line with the high passivation level. In subfigure c), the thickness of the interfacial silicon oxide has been estimated at 1.1 ± 0.2 nm. Note that this is a somewhat lower thickness than would be expected from the ellipsometry result in Fig. 2 (~1.5 nm). Potentially this discrepancy stems from the fact that fixed optical constants were used for the ellipsometry modelling. It is also conceivable there is a real difference in oxide thickness due to a different oxidation rate on the slopes of the pyramid, e.g. due to the different *c*-Si crystal orientation or the enhanced surface area to be oxidized.

What can also be learnt from the contrast in the high angle annular dark field (HAADF) STEM image in Fig. 6 (d) is that the ZnO crystal grains continue across the Al dopant planes. Similar behavior can be observed in the TEM images in the prior work of van de Loo et al., where triisopropyl borate (TIB) was used as boron dopant precursor [74]. This is however distinctly different from what we have previously observed for ALD ZnO:Al doped using TMA [75]. In that case, the introduction of Al atoms by TMA interrupts the crystal growth and new ZnO crystals nucleate after each dopant cycle. This is thought to relate to the fact that when using DMAI or TIB as dopant precursor, much less dopants are introduced per doping cycle as compared to TMA [52]. Specifically, Garcia-Alonso et al. compared the areal dopant density per dopant cycle in ZnO when using TMA, DMAI or TIB as dopant precursor and found values around 8–10, 4–5 and 3–4 at. per $nm^2$, respectively [76].

Fig. 6(d) shows a HR-HAADF-STEM image in which layers of different contrast within the ZnO:Al layer can be discerned, which are attributed to the Al-dopant planes introduced during the supercycle ALD recipe. Fig. 6 (e) and (f) show the image used for EDX mapping and the resulting Al signal, respectively. Also in the Al signal these distinct planes can be discerned. The elemental EDX profile of this cross-section is shown in Fig. 7. Since the dopant planes can be clearly resolved, it can be concluded that the Al dopants do not migrate significantly at annealing temperatures of 400 °C.

A similar sample annealed at 600 °C was investigated by TEM in order to gain insights into the mechanism behind the degradation of the

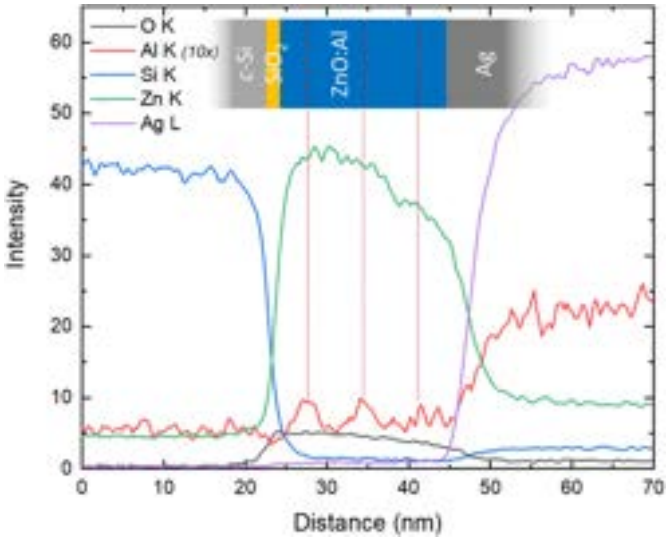


**Fig. 7.** Compositional profile (a.u.) as obtained from EDX mapping of the image in Fig. 6 e) for the sample after annealing at 400 °C. The inset image shows the analyzed stack and the approximate corresponding position in the image. The red lines denote the Al dopant planes originating from the supercycle doping approach. Note that for clarity the Al signal was scaled 10 times and that the heightened Al signal in the Ag area is an artifact due to a raised background. (For interpretation of the references to colour in this figure legend, the reader is referred to the Web version of this article.)

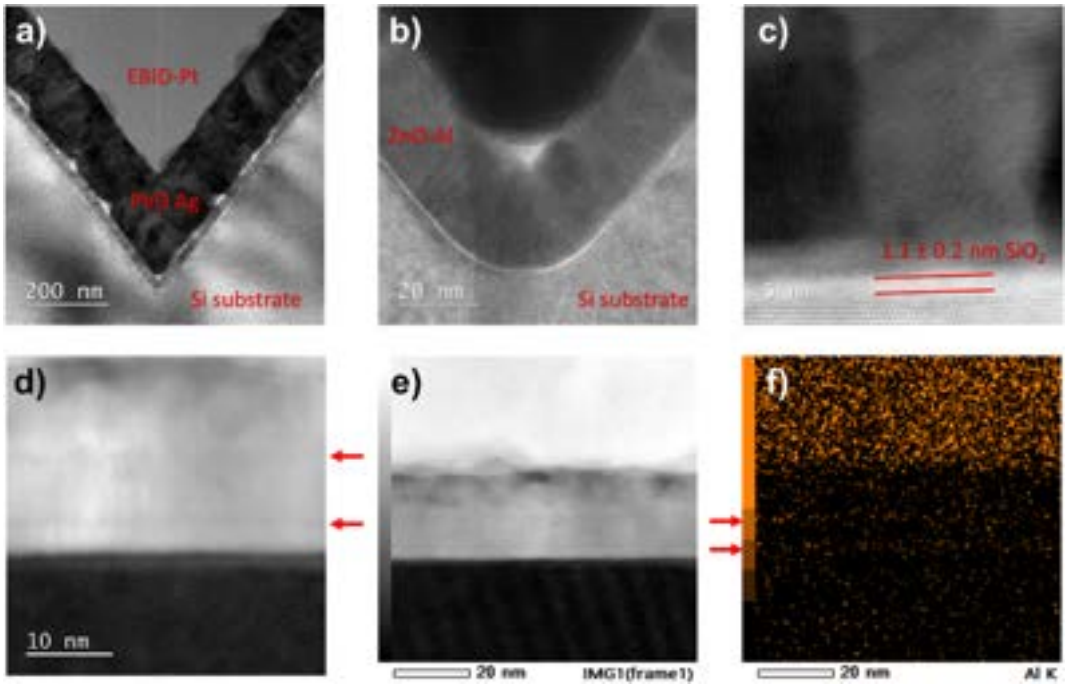


**Fig. 6.** Electron microscopy investigation of the ZnO:Al-based stack after annealing at 400 °C. a) Overview BF-TEM image of the stack in the valley of a pyramid. b) HR-TEM image showing the conformal coating of the valley of the pyramid. c) BF-STEM close-up of the $SiO_2$ layer. d) HR-HAADF-STEM image showing the Al dopant planes. Also, the image reveals that ZnO grain growth is not interrupted by the Al-doping cycle. e) HAADF image used for EDX mapping. F) EDX image of the Al content. The red arrows denote the Al dopant planes that can be discerned. The raised Al signal in the Ag layer is an artifact due to a raised background. (For interpretation of the references to colour in this figure legend, the reader is referred to the Web version of this article.)

surface passivation quality at these temperatures. Note that opposed to the TEM sample annealed at 400 °C, for this sample the $Al_2O_3$ capping layer was not removed after anneal and no Ag layer for contacting was applied. This was done since for the previous sample it was noticed that the Ag layer rendered TEM imaging quite challenging as Ag tends to diffuse during imaging. A collection of illustrative TEM images is displayed in Fig. 8.

From these TEM images, a few key observations can be made. Firstly, the *c*-Si/$SiO_2$ interface appears roughened, and the thickness of the $SiO_2$ interlayer varies in the range of 1.1–1.5 nm. This is reminiscent of $SiO_2$/poly-Si passivating contacts in which thermal stress during high-temperature annealing leads to pinhole formation and even break-up of the oxide due to thermal stress [77,78]. It should however be noted that the loss of passivation observed in this work occurs at relatively lower temperatures of 550–600 °C, whereas the oxide in $SiO_2$/poly-Si contacts typically degrades at temperatures in the range of 750–1050 °C, depending on the oxide preparation method [78]. Nevertheless, whereas *c*-Si and poly-Si have similar coefficients of thermal expansion (CTE), the CTE of c-Si and ZnO is quite different, especially at elevated temperatures. Specifically, the linear CTE of *c*-Si increases from approximately $2.5x10^{-6}$ $K^{-1}$ to $4x10^{-6}$ $K^{-1}$ when going from room temperature to 600 °C [79]. The thermal expansion of ZnO is anisotropic due to the wurtzite crystal structure and is often described using two CTE values, parallel and perpendicular to the c-axis. Both CTE values of ZnO are higher than that of *c*-Si and increase more strongly with temperature. The parallel and perpendicular CTE range from approximately $3x10^{-6}$ $K^{-1}$ and $5x10^{-6}$ $K^{-1}$ at room temperature, to $5x10^{-6}$ $K^{-1}$ and $8x10^{-6}$ $K^{-1}$ at 600 °C, respectively [80]. The relatively higher levels of interfacial stress that are thus expected for the $SiO_2$/ZnO stack compared to $SiO_2$/poly-Si could well be the reason for the disintegration of the $SiO_2$ layer at relatively lower temperatures, and consequently the loss of passivation.

The TEM images also show the appearance of voids in the ZnO:Al, which is accompanied with the protrusion of the ZnO:Al into the $Al_2O_3$ capping layer. The reason for void formation is currently not known, but could be related to a pressure build-up of hydrogen during high-temperature annealing, as the $Al_2O_3$ capping layer prevents the effusion of hydrogen. This would be similar to the formation of so-called blisters, sometimes observed when annealing $Al_2O_3$ films [81]. Importantly, as the next section will show, these films are highly conductive, so the void fraction is insufficient to hamper the percolation significantly.

Compared to the sample annealed at 400 °C, the individual ZnO:Al grains are much easier to discern and appear columnar. Therefore, it appears that the ZnO grains have coarsened, similar as to what has been reported for spatial ALD-prepared ZnO layers annealed at similar temperatures [82]. Interestingly, for this sample the distinct Al dopant planes could no longer be observed. Therefore it is conceivable that the Al dopants have spread over the film as an effect of the anneal treatment. Unfortunately, since the $Al_2O_3$ capping layer overwhelms the Al signal in EDX measurements, the extent of migration of Al dopants into the ZnO:Al film could not be determined.

### 3.4. Lateral conductivity and transparency of the ZnO:Al TCO

It was found that the anneal treatment that is used to activate the passivation can also strongly improve the optical and electronic properties of ALD ZnO:Al layers, provided an $Al_2O_3$ capping layer is present. This is demonstrated using Type D samples (Fig. 1). Samples with and without an $Al_2O_3$ capping layer were prepared and the Al-doping content of the ZnO:Al layer was adjusted by varying the supercycle ratio *n*. As can be seen in Fig. 9 (left), the resistivity of all uncapped layers degrades strongly upon annealing. Interestingly, this degradation is not observed for the capped ZnO:Al layers. The degradation of the uncapped ZnO:Al layers most likely stems from interaction with air, as has also been observed for e.g. $In_2O_3$-based films [83]. The resistivity for the capped ZnO:Al layers gradually improves for annealing temperatures up to about 500 °C, followed by a further improvement for annealing at 550–650 °C. Overall, substantial reductions in the resistivity close to 50% can be obtained for the Al-doped samples. Annealing the Al-doped samples at 700 °C leads to a degradation in resistivity. The latter is not observed for the iZnO sample.

Hall measurements were performed to investigate how the observed

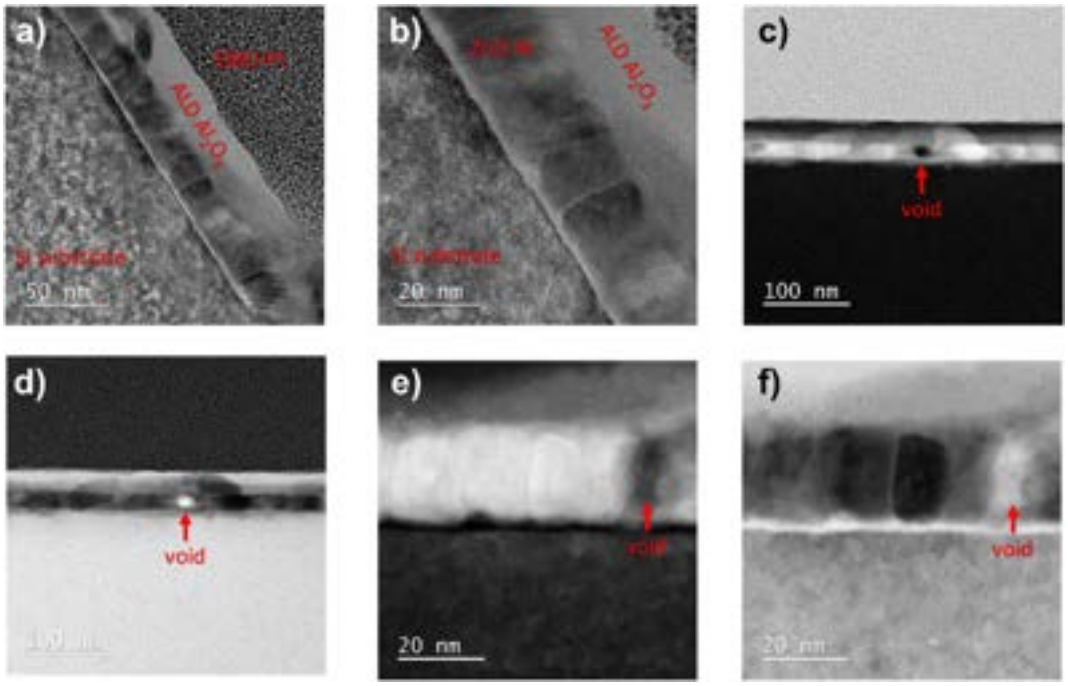


**Fig. 8.** Electron microscopy investigation of the ZnO:Al-based stack after annealing at 600 °C. a,b) Overview BF-TEM image of the stack on the slope of a pyramid, showing the roughened interface and $SiO_2$ interlayer of fluctuating thickness. c,d) STEM images displaying the presence of a void and the protrusion of the ZnO to the $Al_2O_3$ layer. e,f) Close-up complementary HAADF and BF STEM images displaying clear ZnO:Al grains as well as the void.

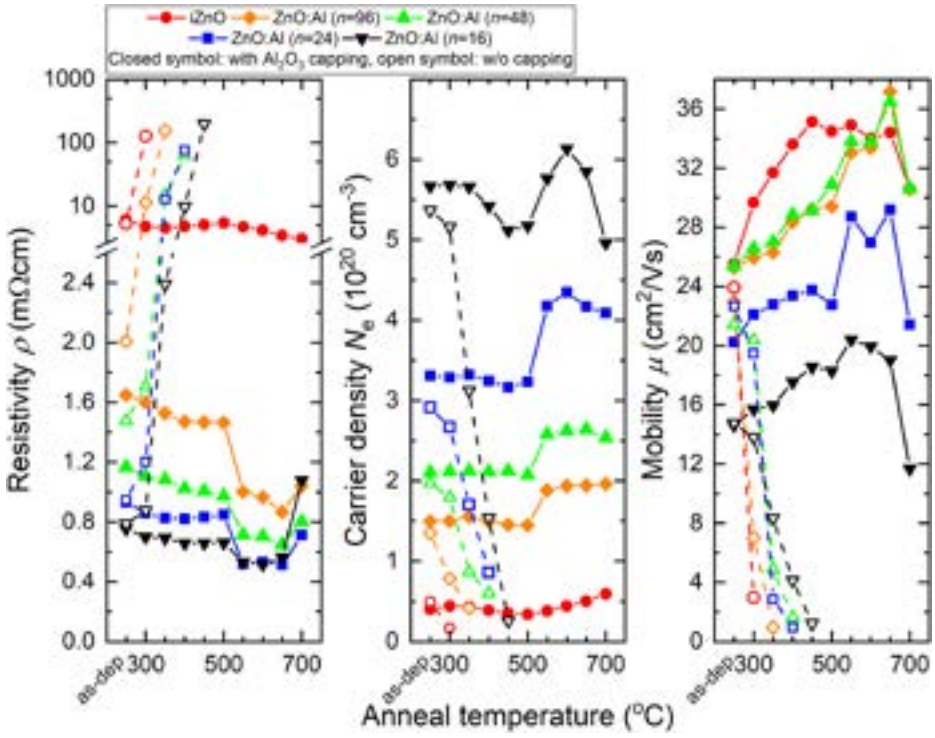


**Fig. 9.** Data from Hall measurements showing the resistivity $\rho$ (left panel), carrier density $N_e$ (middle panel) and carrier mobility $\mu_e$ (right panel) of ALD ZnO:Al layers with various Al-doping levels. Measurements were performed on capped (closed symbol) and uncapped (open symbol) samples. Annealing steps were performed consecutively for 5 min.

trend in resistivity upon annealing relates to changes in the carrier density $N_e$ and mobility $\mu_e$. As expected, in the as-deposited state a higher doping level (i.e. a lower cycle ratio $n$) results in a higher carrier density $N_e$. At the same time, the carrier mobility $\mu_e$ decreases with increasing doping level, which is attributed to a combination of enhanced ionized impurity scattering from active dopants [84], scattering from inactive dopants and possibly increased grain boundary scattering due to a reduction of grain size [75,85]. Upon annealing the uncapped ZnO:Al samples, a strong reduction in both carrier density and mobility is observed. Although the precise mechanism is not known, the fact that this degradation does not occur for capped ZnO:Al layers points to effusion of hydrogen or interaction with ambient gas being the main culprit. Also note that Hall measurements were unsuccessful for uncapped ZnO:Al layers annealed at elevated temperatures and that the samples started to visually degrade. The carrier density of the capped ZnO:Al samples is relatively constant upon annealing up to 500 °C, followed by an increase in carrier density when annealing at higher temperatures. Potentially this increase in carrier density is related to diffusion of Al dopants away from the Al-dopant planes as was seen in the TEM images in Fig. 8. Since clustered Al dopants tend to be inactive, more uniform spreading of the Al atoms would enhance the carrier density [52]. The carrier mobility of all capped samples shows a substantial and monotonic improvement for annealing up to 650 °C. Multiple factors are thought to contribute to this enhanced mobility. Firstly, since the $Al_2O_3$ capping layer is known to prevent effusion of hydrogen at these temperatures, the main hypothesis is that similarly as for surface passivation, hydrogen plays a crucial role in improving the carrier mobility. Indeed, hydrogen has been widely argued to passivate defects and traps at grain boundaries, most notably in polycrystalline silicon and TCOs [86–88]. As such, H-doped TCOs such as ZnO:H and $In_2O_3$:H exhibit among the highest carrier mobility values [41,42,86,89]. In addition, the TEM images point to recrystallization into larger and differently oriented grains during annealing. This increase in grain size contributes to an improvement in mobility due to reduced grain boundary scattering. Finally, spreading of the Al dopants out of their dopant planes can help contribute to a higher mobility, since ionized impurity scattering is minimized when dopants are spread isotropically [84]. Altogether, these measurements demonstrate that the reduction in resistivity of the capped ZnO:Al samples upon annealing mostly stems from an improvement in mobility, accompanied by an increase in carrier density.

In addition to improving the electrical resistivity, the presence of the $Al_2O_3$ capping layer during annealing also helps to improve the optical transparency of the ZnO:Al layers considerably. Spectroscopic ellipsometry has been used to determine the spectral optical constants and to examine the Drude parameters. For clarity of presentation, the resulting spectral absorption coefficient $\alpha$ is shown rather than the full refractive index and extinction coefficient data. Fig. 10 shows the absorption coefficient $\alpha$ for capped samples for the various Al-doping cycle ratios $n$. These samples and the anneal treatments correspond to the samples reported in Fig. 9.

Focusing on the low-energy part of the spectra, it is apparent that higher doping levels lead to a higher absorption coefficient. This stems from the Drude response, which is given by [57]:

$$\varepsilon_{Drude}(\omega) = -\frac{\omega_p^2}{\omega^2 + i\omega\omega_\tau}, \quad \omega_p = \sqrt{\frac{e^2 N_e}{\varepsilon_0 m^*}}, \quad \omega_\tau = \frac{e}{m^* \mu} \tag{1}$$

In these equations, $\omega$ is the frequency, i the imaginary number, $e$ the elementary charge, $m^*$ the effective electron mass and $\varepsilon_0$ the permittivity of free space. Briefly put, the plasma frequency $\omega_p$ determines the onset of the Drude response, whereas the scatter frequency $\omega_\tau$ determines the broadening of the response above the plasma frequency.

Upon annealing, the Drude response progressively decreases for all doped samples. To quantify this effect, the plasma frequency $\omega_p$ and scatter frequency $\omega_\tau$ have been determined from the Drude response and are shown in Fig. 11. The plasma frequency is relatively constant for annealing up to 500 °C, followed by a small increase. As the plasma frequency mainly depends on the carrier density, this is in line with the carrier density results from the Hall measurements. The scatter

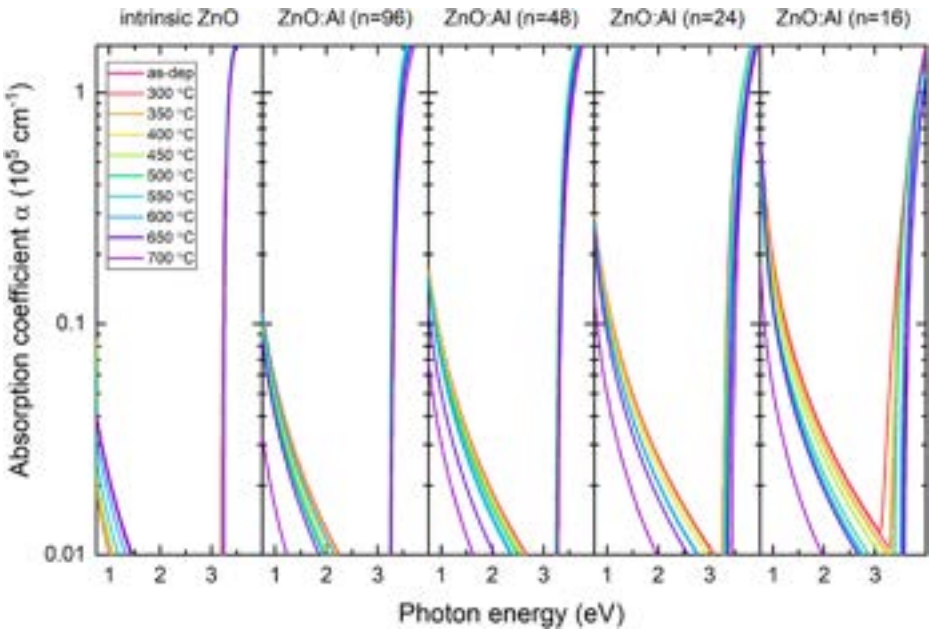


**Fig. 10.** Absorption coefficient of ZnO:Al films and the effect of thermal annealing thereon. Data are shown for capped ZnO:Al samples of various Al-doping levels.

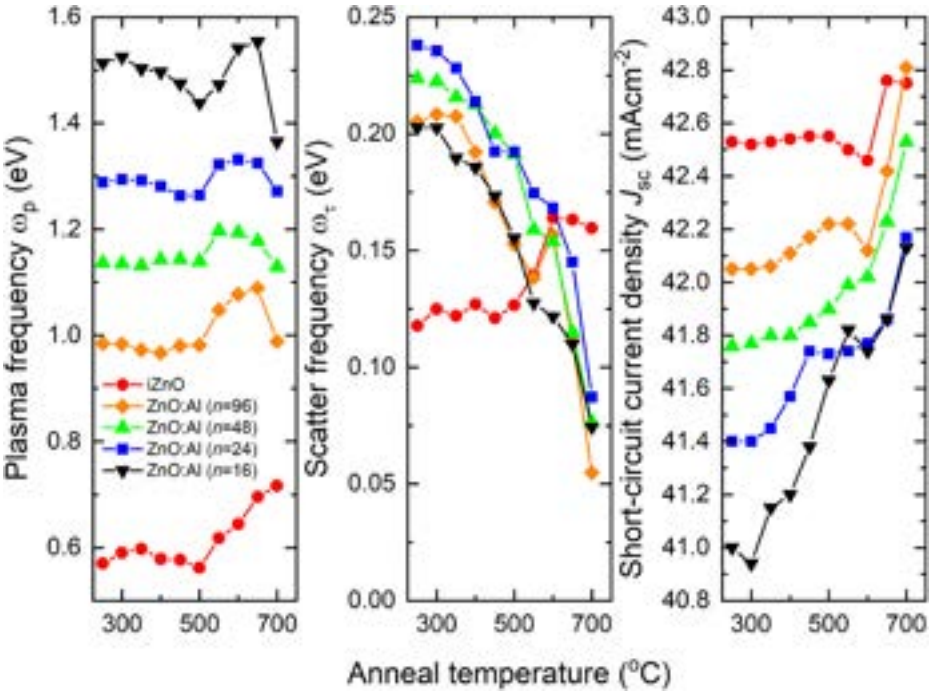


**Fig. 11.** The plasma frequency $\omega_p$ (left), scatter frequency $\omega_\tau$ (middle) and short-circuit current density $J_{sc}$ as obtained from optical modelling (right). Data are shown for capped ZnO:Al samples of various Al-doping levels.

frequency of the Al-doped samples strongly decreases upon annealing. Interestingly, upon annealing at 700 °C the scatter frequency continues to reduce whereas the Hall mobility shows a strong decrease. This effect is also seen in Fig. S2 of the Supplementary Information, where the optical and electrical mobility are compared. It can be seen that the optical and electrical mobility are comparable for Al-doped films up to an annealing temperature of ~600–650 °C, after which the optical mobility still increases strongly while the electrical mobility degrades. Unlike Hall measurements, SE measurements are insensitive to scattering at longer length scales such as at grain boundaries [57]. Because of this, it is hypothesized that for the ZnO:Al samples, the reduction of Hall mobility occurring at high annealing temperatures can be due to segregation of Al into e.g. $Al_2O_3$ clusters at the grain boundaries [85].

In order to substantiate the potential optical performance of the capped ZnO:Al samples and to see to which extent the reduction in Drude response upon annealing can contribute to this, the expected $J_{sc}$ when using these TCOs as an antireflection coating on textured *c*-Si has been simulated. Specifically, a structure consisting of a 180 μm thick, random-pyramid textured *c*-Si substrate with a stack consisting of 1 nm $SiO_2$/75 nm ZnO:Al/30 nm $Al_2O_3$ has been simulated using PVLighthouse OPAL2 and the photocurrent generated in the *c*-Si substrate was taken as the $J_{sc}$ [55]. Front metal shading losses were assumed to be

absent. The optical constants *n&k* of the ZnO:Al layers as obtained from spectroscopic ellipsometry were taken as input. As Fig. 11 (right) shows, in the as-deposited state a higher ZnO:Al doping level results in a lower simulated $J_{sc}$, which is attributed to stronger Drude losses. Upon annealing the simulated $J_{sc}$ improves considerably, especially for the most highly doped samples, yielding improvements up to 1 mA/cm$^2$. In order to put these results in perspective, a comparison was made to various TCO materials and a standard PECVD $SiN_x$ antireflection coating, using *n&k* and resistivity values reported in literature. In Fig. 12, the resulting $J_{sc}$ values for the capped ZnO:Al layers have been plotted as a function of layer resistivity. The figure clearly shows that the annealing treatment is effective in improving both the electrical conductivity and the $J_{sc}$. Interestingly, this treatment brings the performance of the ZnO TCOs into the regime typically only obtainable using ITO and IZO, although the performance of the high-mobility $In_2O_3$:H TCO is still out of reach. Nevertheless, in light of the active pursuit of Zn-based TCOs as an abundant replacement for the scarce In-based TCOs, these results show that using an $Al_2O_3$ capping layer and subsequent annealing can be a more generally applicable approach to bring the performance of ZnO-based TCOs on par with that of their In-based counterparts [72].

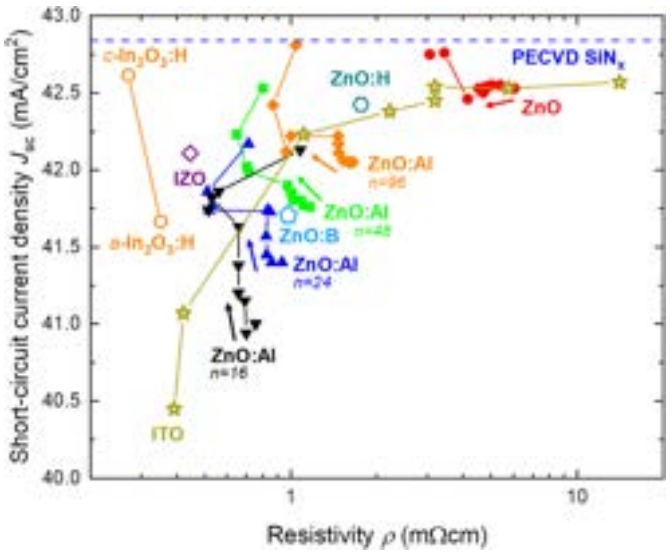


**Fig. 12.** Plot of the simulated short-circuit current density $J_{sc}$ as a function of the TCO resistivity $\rho$. Optical simulations were performed using the OPAL2 calculator of PV Lighthouse [55], assuming a on random-pyramid textured *c*-Si. Full symbols correspond to data from this work, open symbols refer to data generated from the literature. Data are shown for the capped ZnO:Al samples as a function of annealing temperature. The arrows denote the direction of the annealing steps, corresponding to the annealing procedure in Fig. 10. Using reported literature data (*n&k* and resistivity), datapoints for PECVD $SiN_x$ [90], PVD ITO [91], PVD IZO [38], ALD ZnO:B [49], ALD ZnO:H [42] and amorphous and crystallized ALD $In_2O_3$:H [41] have been added.

## 4. Conclusions and outlook

In this work it is shown that stacks consisting of ALD ZnO(:Al)/$Al_2O_3$ on a thin $SiO_2$ layer can provide a combination of functionalities relevant for solar cell operation. Specifically, these stacks are shown to be highly passivating, conductive, transparent, relatively thermally stable and moreover capable of electrically contacting $n^+$-diffused *c*-Si surfaces.

With respect to surface passivation, it was found that the stacks can give high i$V_{oc}$ values of 728 mV on random-pyramid textured *c*-Si as well as on planar, mirror-polished surfaces. Moreover, the passivation level on $n^+$-diffused surfaces is comparable to that of other common surface passivation schemes. By comparing different methods to prepare the interfacial $SiO_x$ layer, it was found that the UV/$O_3$, NAOS and RCA approaches yield almost equally excellent passivation and that the passivating stack is thermally stable up to approximately 550–600 °C. As such, the passivating stack can withstand relatively high temperatures compared to most passivating and contacting layers, yet it is not firing-stable.

It was additionally found that low contact resistivities could be obtained on $n^+$-diffused Si surfaces as well as on poly-Si(*n*) contacts. The doping level of both the ZnO:Al as well as the *c*-Si were demonstrated to be crucial for obtaining a low contact resistivity. Excellent values down to 15, 23 and 42 mΩcm$^2$ were obtained on 130 Ω/sq $n^+$-diffused Si, 260 Ω/sq $n^+$-diffused Si and poly-Si(*n*) surfaces, respectively.

The $Al_2O_3$ capping layer, which plays a vital role in surface passivation by preventing the effusion of hydrogen during the post-deposition annealing, was additionally shown to enable a substantial improvement in both the conductivity and transparency of the ZnO:Al layers. Hall measurements show that the capped samples mainly benefit from a strong improvement in carrier mobility, which is thought to originate from H-induced passivation of defects in the ZnO:Al layer, grain coarsening leading to larger grains, as well as more uniform spreading of Al dopants in the film. In line with the Hall results, analysis of the Drude response shows that the annealing treatment of the capped samples leads to a strong reduction of the free carrier absorption. Using optical simulations and through a comparison with common TCO materials reported in literature, it is shown that the annealing treatment improves the optical and electrical properties of capped ZnO:Al layers to a level that is typically only attainable by In-based TCOs.

In summary, this work demonstrates that ZnO-based stacks are capable of simultaneously providing multiple device-relevant functionalities, and vital steps to arrive at these properties are outlined. Future work should focus on working towards device integration of the presented stack. One evident device application would be to use the ZnO-based stack as a full-area passivating and contacting layer on the front side of a PERC-type solar cell, replacing the $SiN_x$ layer. The full-area passivation provided by the ZnO would render shielding of minority carriers by the $n^+$-diffused region much less critical, while simultaneously providing an additional lateral current path for electron extraction. Both effects can possibly reduce the required $n^+$ doping level in the emitter and thereby, together with the absence of a direct Si-metal contact, enable a higher $V_{oc}$. Additionally, the integration of a front TCO on a PERC cell is an important step towards enabling PERC cells to be used as bottom cells in silicon-perovskite tandem cells. Finally, the ZnO/$Al_2O_3$ stack is a highly attractive In-free TCO for poly-Si passivating contacts, in which the anneal treatment can serve a dual function. i.e. to improve the ZnO properties and for hydrogenation of the $SiO_2$ interlayer.

## CRediT authorship contribution statement

**Bart Macco:** Conceptualization, Methodology, Investigation, Writing – original draft, Writing – review & editing, Visualization, Supervision, Project administration, Funding acquisition. **Bas W.H. van de Loo:** Conceptualization, Writing – review & editing. **Marc Dielen:** Investigation. **Dennis G.J.A. Loeffen:** Investigation. **Bart B. van Pelt:** Methodology, Investigation, Writing – review & editing. **Nga Phung:** Investigation, Writing – review & editing. **Jimmy Melskens:** Writing – review & editing. **Marcel A. Verheijen:** Investigation, Writing – review & editing. **Wilhelmus M.M. Kessels:** Writing – review & editing, Supervision, Project administration, Funding acquisition.

## Declaration of competing interest

The authors declare that they have no known competing financial interests or personal relationships that could have appeared to influence the work reported in this paper.

## Acknowledgements

The authors acknowledge J. J. L. M. Meulendijks, C. O. van Bommel, C.A.A. van Helvoirt, J. van Gerwen and J. J. A. Zeebregts for their technical support.. The authors gratefully acknowledge Solliance for funding the TEM facility and dr. B. Barcones-Campo for the TEM sample preparation. The authors acknowledge the project partners TNO and Tempress Systems, and especially dr. L.J. Geerligs of TNO for providing the LPCVD poly-Si samples. We acknowledge financial support for this research from the Top consortia for Knowledge and Innovation (TKI) Solar Energy program "PERCspective" (TEUE119005) and "SATURNIA" (TEUE118002) of the Ministry of Economic Affairs of The Netherlands. The work of B. Macco and J. Melskens was supported by The Netherlands Organization for Scientific Research under the Dutch TTW-VENI Grants 16775 and 15896, respectively.

## Appendix A. Supplementary data

Supplementary data to this article can be found online at https://doi.org/10.1016/j.solmat.2021.111386.

## References

[1] A. Richter, M. Hermle, S.W. Glunz, Reassessment of the limiting efficiency for crystalline silicon solar cells, IEEE J. Photovoltaics 3 (2013) 1184–1191, https://doi.org/10.1109/JPHOTOV.2013.2270351.

[2] J. Melskens, B.W.H. van de Loo, B. Macco, L.E. Black, S. Smit, W.M.M. Kessels, Passivating contacts for crystalline silicon solar cells: from concepts and materials to prospects, IEEE J. Photovoltaics. 8 (2018) 373–388, https://doi.org/10.1109/JPHOTOV.2018.2797106.

[3] B. Macco, B.W.H. van de Loo, W.M.M. Kessels, Atomic Layer Deposition for High Efficiency Crystalline Silicon Solar Cells, Wiley, 2017.

[4] R. Brendel, R. Peibst, Contact selectivity and efficiency in crystalline silicon photovoltaics, IEEE J. Photovoltaics. 6 (2016) 1413–1420, https://doi.org/10.1109/JPHOTOV.2016.2598267.

[5] U. Wurfel, A. Cuevas, P. Wurfel, Charge carrier separation in solar cells, IEEE J. Photovoltaics. 5 (2015) 461–469, https://doi.org/10.1109/JPHOTOV.2014.2363550.

[6] T.G. Allen, J. Bullock, X. Yang, A. Javey, S. De Wolf, Passivating contacts for crystalline silicon solar cells, Nat. Energy. (2019) 2–3, https://doi.org/10.1038/s41560-019-0463-6.

[7] A. Cuevas, T. Allen, J. Bullock, Yimao Wan, Di, Xinyu Zhang, Skin care for healthy silicon solar cells, in: 2015 IEEE 42nd Photovolt. Spec. Conf., IEEE, 2015: pp. 1-6. https://doi.org/10.1109/PVSC.2015.7356379.

[8] G. Dingemans, W.M.M. Kessels, Status and prospects of $Al_2O_3$-based surface passivation schemes for silicon solar cells, J. Vac. Sci. Technol. A Vacuum, Surfaces, Film. 30 (2012), 040802, https://doi.org/10.1116/1.4728205.

[9] R.S. Bonilla, B. Hoex, P. Hamer, P.R. Wilshaw, Dielectric surface passivation for silicon solar cells: a review, Phys. Status Solidi Appl. Mater. Sci. 214 (2017), https://doi.org/10.1002/pssa.201700293.

[10] A. Richter, S.W. Glunz, F. Werner, J. Schmidt, A. Cuevas, Improved quantitative description of Auger recombination in crystalline silicon, Phys. Rev. B 86 (2012) 1–14, https://doi.org/10.1103/PhysRevB.86.165202.

[11] A. Cuevas, Y. Wan, D. Yan, C. Samundsett, T. Allen, X. Zhang, J. Cui, J. Bullock, Carrier population control and surface passivation in solar cells, Sol. Energy Mater. Sol. Cells 184 (2018) 38–47, https://doi.org/10.1016/j.solmat.2018.04.026.

[12] U. Jäger, S. Mack, C. Wufka, A. Wolf, D. Biro, R. Preu, Benefit of selective emitters for p-type silicon solar cells with passivated surfaces, IEEE J. Photovoltaics. 3 (2013) 621–627, https://doi.org/10.1109/JPHOTOV.2012.2230685.

[13] M. Kondo, S. De Wolf, H. Fujiwara, Understanding of passivation mechanism in heterojunction c-Si solar cells, MRS Proc 1066 (2011), https://doi.org/10.1557/PROC-1066-A03-01.

[14] R. van der Vossen, F. Feldmann, A. Moldovan, M. Hermle, Comparative study of differently grown tunnel oxides for p-type passivating contacts, Energy Procedia 124 (2017) 448–454, https://doi.org/10.1016/j.egypro.2017.09.273.

[15] A. Moldovan, F. Feldmann, M. Zimmer, J. Rentsch, J. Benick, M. Hermle, Tunnel oxide passivated carrier-selective contacts based on ultra-thin $SiO_2$ layers, Sol. Energy Mater. Sol. Cells 142 (2015) 123–127, https://doi.org/10.1016/j.solmat.2015.06.048.

[16] F. Haase, F. Kiefer, S. Schäfer, C. Kruse, J. Krügener, R. Brendel, R. Peibst, Interdigitated back contact solar cells with polycrystalline silicon on oxide passivating contacts for both polarities, Jpn. J. Appl. Phys. 56 (2017), 08MB15, https://doi.org/10.7567/JJAP.56.08MB15.

[17] M. Schnabel, B.W.H. Van De Loo, W. Nemeth, B. Macco, P. Stradins, W.M.M. Kessels, D.L. Young, Hydrogen passivation of poly-Si/$SiO_x$ contacts for Si solar cells using $Al_2O_3$ studied with deuterium, Appl. Phys. Lett. 112 (2018), https://doi.org/10.1063/1.5031118.

[18] B. Macco, J. Melskens, N.J.N.J. Podraza, K. Arts, C. Pugh, O. Thomas, W.M.M. Kessels, Correlating the silicon surface passivation to the nanostructure of low-temperature a-Si:H after rapid thermal annealing, J. Appl. Phys. 122 (2017), 035302, https://doi.org/10.1063/1.4994795.

[19] F. Feldmann, M. Bivour, C. Reichel, H. Steinkemper, M. Hermle, S.W. Glunz, Tunnel oxide passivated contacts as an alternative to partial rear contacts, Sol. Energy Mater. Sol. Cells 131 (2014) 46–50, https://doi.org/10.1016/j.solmat.2014.06.015.

[20] S. De Wolf, A. Descoeudres, Z.C. Holman, C. Ballif, High-efficiency silicon heterojunction solar cells: a review, Green 2 (2012) 7–24, https://doi.org/10.1515/green-2011-0018.

[21] M. Köhler, M. Pomaska, P. Procel, R. Santbergen, A. Zamchiy, B. Macco, A. Lambertz, W. Duan, P. Cao, B. Klingebiel, S. Li, A. Eberst, M. Luysberg, K. Qiu, O. Isabella, F. Finger, T. Kirchartz, U. Rau, K. Ding, A silicon carbide-based highly transparent passivating contact for crystalline silicon solar cells approaching efficiencies of 24%, Nat. Energy. (2021) https://doi.org/10.1038/s41560-021-00806-9.

[22] L.G. Gerling, S. Mahato, A. Morales-Vilches, G. Masmitja, P. Ortega, C. Voz, R. Alcubilla, J. Puigdollers, Transition metal oxides as hole-selective contacts in silicon heterojunctions solar cells, Sol. Energy Mater. Sol. Cells (2015) 1–7, https://doi.org/10.1016/j.solmat.2015.08.028.

[23] G. Masmitjà, L.G. Gerling, P. Ortega, J. Puigdollers, I. Martín, C. Voz, R. Alcubilla, $V_2O_x$-based hole-selective contacts for c-Si interdigitated back-contacted solar cells, J. Mater. Chem. A. 5 (2017) 9182, https://doi.org/10.1039/C7TA01959A. –9189.

[24] M. Mews, L. Korte, B. Rech, Oxygen vacancies in tungsten oxide and their influence on tungsten oxide/silicon heterojunction solar cells, Sol. Energy Mater. Sol. Cells (2016) 1–7, https://doi.org/10.1016/j.solmat.2016.05.042.

[25] B. Macco, M.F.J. Vos, N.F.W. Thissen, A.A. Bol, W.M.M. Kessels, Low-temperature atomic layer deposition of $MoO_x$ for silicon heterojunction solar cells, Phys. Status Solidi Rapid Res. Lett. 9 (2015) 393–396, https://doi.org/10.1002/pssr.201510117.

[26] M. Bivour, B. Macco, J. Temmler, M. Hermle, W.M.M. Kessels, Atomic layer deposited molybdenum oxide for the hole-selective contact of silicon solar cells, Energy Procedia 92 (2016) 443–449, https://doi.org/10.1016/j.egypro.2016.07.125.

[27] J. Geissbühler, J. Werner, S. Martin de Nicolas, L. Barraud, A. Hessler-Wyser, M. Despeisse, S. Nicolay, A. Tomasi, B. Niesen, S. De Wolf, C. Ballif, 22.5% efficient silicon heterojunction solar cell with molybdenum oxide hole collector, Appl. Phys. Lett. 107 (2015), 081601, https://doi.org/10.1063/1.4928747.

[28] M. Bivour, J. Temmler, H. Steinkemper, M. Hermle, Molybdenum and tungsten oxide: high work function wide band gap contact materials for hole selective contacts of silicon solar cells, Sol. Energy Mater. Sol. Cells 142 (2015) 34–41, https://doi.org/10.1016/j.solmat.2015.05.031.

[29] J. Dréon, Q. Jeangros, J. Cattin, J. Haschke, L. Antognini, C. Ballif, M. Boccard, 23.5%-Efficient silicon heterojunction silicon solar cell using molybdenum oxide as hole-selective contact, Nano Energy 70 (2020), https://doi.org/10.1016/j.nanoen.2020.104495.

[30] M. Mews, A. Lemaire, L. Korte, Sputtered tungsten oxide as hole contact for silicon heterojunction solar cells, IEEE J. Photovoltaics (2017) 1–7, https://doi.org/10.1109/JPHOTOV.2017.2714193.

[31] X. Yang, Q. Bi, H. Ali, K. Davis, W.V. Schoenfeld, K. Weber, High-performance $TiO_2$-based electron-selective contacts for crystalline silicon solar cells, Adv. Mater. 28 (2016) 5891–5897, https://doi.org/10.1002/adma.201600926.

[32] X. Yang, K. Weber, Z. Hameiri, S. De Wolf, Industrially feasible, dopant-free, carrier-selective contacts for high-efficiency silicon solar cells, Prog. Photovoltaics Res. Appl. 25 (2017) 896–904, https://doi.org/10.1002/pip.2901.

[33] B. Macco, L.E. Black, J. Melskens, B.W.H. van de Loo, W.J.H. Berghuis, M. A. Verheijen, W.M.M. Kessels, Atomic-layer deposited $Nb_2O_5$ as transparent passivating electron contact for c-Si solar cells, Sol. Energy Mater. Sol. Cells 184 (2018), https://doi.org/10.1016/j.solmat.2018.04.037.

[34] Z.C. Holman, A. Descoeudres, L. Barraud, F.Z. Fernandez, J.P. Seif, S. De Wolf, C. Ballif, Current losses at the front of silicon heterojunction solar cells, IEEE J. Photovoltaics. 2 (2012) 7–15, https://doi.org/10.1109/JPHOTOV.2011.2174967.

[35] S. Essig, J. Dréon, E. Rucavado, M. Mews, T. Koida, M. Boccard, J. Werner, J. Geissbühler, P. Löper, M. Morales-Masis, L. Korte, S. De Wolf, C. Ballif, Toward annealing-stable molybdenum-oxide-based hole-selective contacts for silicon photovoltaics, Sol. RRL. 2 (2018) 1700227, https://doi.org/10.1002/solr.201700227.

[36] D. Sacchetto, Q. Jeangros, G. Christmann, L. Barraud, A. Descoeudres, J. Geissbuhler, M. Despeisse, A. Hessler-Wyser, S. Nicolay, C. Ballif, ITO/$MoO_x$/a-Si:H(i) hole-selective contacts for silicon heterojunction solar cells: degradation mechanisms and cell integration, IEEE J. Photovoltaics. 7 (2017) 1584–1590, https://doi.org/10.1109/JPHOTOV.2017.2756066.

[37] T. Koida, H. Fujiwara, M. Kondo, High-mobility hydrogen-doped $In_2O_3$ transparent conductive oxide for a-Si:H/c-Si heterojunction solar cells, Sol. Energy Mater. Sol. Cells 93 (2009) 851–854, https://doi.org/10.1016/j.solmat.2008.09.047.

[38] M. Morales-Masis, S. Martin De Nicolas, J. Holovsky, S. De Wolf, C. Ballif, Low-temperature high-mobility amorphous IZO for silicon heterojunction solar cells, IEEE J. Photovoltaics. 5 (2015) 1340–1347, https://doi.org/10.1109/JPHOTOV.2015.2450993.

[39] M. Morales-Masis, S. De Wolf, R. Woods-Robinson, J.W. Ager, P.C. Ballif, Transparent Electrodes for Efficient Optoelectronics, 2017.

[40] B. Macco, Y. Wu, D. Vanhemel, W.M.M. Kessels, High mobility $In_2O_3$:H transparent conductive oxides prepared by atomic layer deposition and solid phase crystallization, Phys. Status Solidi Rapid Res. Lett. 8 (2014) 987–990, https://doi.org/10.1002/pssr.201409426.

[41] B. Macco, H.C.M. Knoops, W.M.M. Kessels, Electron scattering and doping mechanisms in solid-phase-crystallized $In_2O_3$:H prepared by atomic layer deposition, ACS Appl. Mater. Interfaces 7 (2015) 16723–16729, https://doi.org/10.1021/acsami.5b04420.

[42] B. Macco, H.C.M. Knoops, M.A. Verheijen, W. Beyer, M. Creatore, W.M.M. Kessels, Atomic layer deposition of high-mobility hydrogen-doped zinc oxide, Sol. Energy Mater. Sol. Cells 173 (2017) 111–119, https://doi.org/10.1016/j.solmat.2017.05.040.

[43] J. Yu, J. Bian, W. Duan, Y. Liu, J. Shi, F. Meng, Z. Liu, Tungsten doped indium oxide film: ready for bifacial copper metallization of silicon heterojunction solar cell, Sol. Energy Mater. Sol. Cells 144 (2016) 359–363, https://doi.org/10.1016/j.solmat.2015.09.033.

[44] S. Zhong, J. Dréon, Q. Jeangros, E. Aydin, S. De Wolf, F. Fu, M. Boccard, C. Ballif, Mitigating plasmonic absorption losses at rear electrodes in high-efficiency silicon solar cells using dopant-free contact stacks, Adv. Funct. Mater. 30 (2020) 1–9, https://doi.org/10.1002/adfm.201907840.

[45] W. Lin, M. Boccard, S. Zhong, V. Paratte, Q. Jeangros, L. Antognini, J. Dréon, J. Cattin, J. Thomet, Z. Liu, Z. Chen, Z. Liang, P. Gao, H. Shen, C. Ballif, Degradation mechanism and stability improvement of dopant-free ZnO/$LiF_x$/Al electron nanocontacts in silicon heterojunction solar cells, ACS Appl. Nano Mater. 3 (2020) 11391–11398, https://doi.org/10.1021/acsanm.0c02475.

[46] J. Ding, Y. Zhou, G. Dong, M. Liu, D. Yu, F. Liu, Solution-processed ZnO as the efficient passivation and electron selective layer of silicon solar cells, Prog. Photovoltaics Res. Appl. (2018), https://doi.org/10.1002/pip.3044.

[47] L. Tutsch, F. Feldmann, B. Macco, M. Bivour, E. Kessels, W.M.M. Hermle, Improved passivation of n-type poly-Si based passivating contacts by the application of hydrogen-rich transparent conductive oxides, IEEE J. Photovoltaics 10 (2020) 986–991, https://doi.org/10.1109/JPHOTOV.2020.2992348.

[48] B.W.H. van de Loo, B. Macco, M. Schnabel, M.K. Stodolny, A.A. Mewe, D.L. Young, W. Nemeth, P. Stradins, W.M.M. Kessels, On the hydrogenation of Poly-Si passivating contacts by $Al_2O_3$ and $SiN_x$ thin films, Sol. Energy Mater. Sol. Cells 215 (2020) 110592, https://doi.org/10.1016/j.solmat.2020.110592.

[49] B.W.H. van de Loo, B. Macco, J. Melskens, W. Beyer, W.M.M. Kessels, Silicon surface passivation by transparent conductive zinc oxide, J. Appl. Phys. 125 (2019) 105305, https://doi.org/10.1063/1.5054166.

[50] K.G. Sun, Y.V. Li, D.B. Saint John, T.N. Jackson, PH-controlled selective etching of $Al_2O_3$ over ZnO, ACS Appl. Mater. Interfaces 6 (2014) 7028–7031, https://doi.org/10.1021/am501912q.

[51] V.D. Mihailetchi, Y. Komatsu, L.J. Geerligs, Nitric acid pretreatment for the passivation of boron emitters for n-type base silicon solar cells, Appl. Phys. Lett. 92 (2008), 063510, https://doi.org/10.1063/1.2870202.

[52] Y. Wu, S.E. Potts, P.M. Hermkens, H.C.M. Knoops, F. Roozeboom, W.M.M. Kessels, Enhanced doping efficiency of Al-doped ZnO by atomic layer deposition using dimethylaluminum isopropoxide as an alternative aluminum precursor, Chem. Mater. 25 (2013) 4619–4622, https://doi.org/10.1021/cm402974j.

[53] H.C.M. Knoops, S.E. Potts, A.A. Bol, W.M.M. Kessels, Atomic Layer Deposition, second ed., Elsevier B.V., 2015 https://doi.org/10.1016/B978-0-444-63304-0.00027-5.

[54] B. Macco, D. Deligiannis, S. Smit, R.A.C.M.M. van Swaaij, M. Zeman, W.M.M. Kessels, Influence of transparent conductive oxides on passivation of a-Si:H/c-Si heterojunctions as studied by atomic layer deposited Al-doped ZnO, Semicond. Sci. Technol. 29 (2014) 122001, https://doi.org/10.1088/0268-1242/29/12/122001.

[55] K.R. McIntosh, S.C. Baker-Finch, OPAL 2: Rapid optical simulation of silicon solar cells, in: 2012 38th IEEE Photovolt. Spec. Conf., IEEE, 2012: pp. 000265-000271. https://doi.org/10.1109/PVSC.2012.6317616.

[56] D.E. Kane, R.M. Swanson, Measurement of the emitter saturation current by a contactless photoconductivity decay method. 18th IEEE Photovolt. Spec. Conf., Las Vegas, 1985, p. 578.

[57] H.C.M. Knoops, B.W.H. van de Loo, S. Smit, M.V. Ponomarev, J.W. Weber, K. Sharma, W.M.M. Kessels, M. Creatore, Optical modeling of plasma-deposited ZnO films: electron scattering at different length scales, J. Vac. Sci. Technol. A Vacuum, Surfaces, Film. 33 (2015), 021509, https://doi.org/10.1116/1.4905086.

[58] J.I. Polzin, F. Feldmann, B. Steinhauser, M. Hermle, S.W. Glunz, Study on the interfacial oxide in passivating contacts, AIP Conf. Proc. 2147 (2019), https://doi.org/10.1063/1.5123843.

[59] D. Gerlach, M. Wimmer, R.G. Wilks, R. Félix, F. Kronast, F. Ruske, M. Bär, The complex interface chemistry of thin-film silicon/zinc oxide solar cell structures, Phys. Chem. Chem. Phys. 16 (2014) 26266–26272, https://doi.org/10.1039/c4cp03364g.

[60] C. Becker, M. Pagels, C. Zachäus, B. Pollakowski, B. Beckhoff, B. Kanngießer, B. Rech, Chemical speciation at buried interfaces in high-temperature processed polycrystalline silicon thin-film solar cells on ZnO:Al, J. Appl. Phys. 113 (2013), 044519, https://doi.org/10.1063/1.4789599.

[61] S. De Wolf, M. Kondo, Boron-doped a-Si:H/c-Si interface passivation: degradation mechanism, Appl. Phys. Lett. 91 (2007) 112109, https://doi.org/10.1063/1.2783972.

[62] J. Melskens, A.H.M. Smets, M. Schouten, S.W.H. Eijt, H. Schut, M. Zeman, New insights in the nanostructure and defect states of hydrogenated amorphous silicon obtained by annealing, IEEE J. Photovoltaics 3 (2013) 65–71, https://doi.org/10.1109/JPHOTOV.2012.2226870.

[63] J. Melskens, S.W.H. Eijt, M. Schouten, A.S. Vullers, A. Mannheim, H. Schut, B. Macco, M. Zeman, A.H.M. Smets, Migration of open volume deficiencies in hydrogenated amorphous silicon during annealing, IEEE J. Photovoltaics. 7 (2017) 421–429, https://doi.org/10.1109/JPHOTOV.2016.2646421.

[64] T. Zhang, C. Lee, B. Gong, B. Hoex, Thermal Stability Analysis of $WO_x$ and $MoO_x$ as Hole-Selective Contacts for Si Solar Cells Using in Situ XPS, 2018, 040027.

[65] L. Neusel, M. Bivour, M. Hermle, Selectivity issues of $MoO_x$ based hole contacts, Energy Procedia 124 (2017) 425–434, https://doi.org/10.1016/j.egypro.2017.09.268.

[66] M.J. Kerr, J. Schmidt, A. Cuevas, J.H. Bultman, Surface recombination velocity of phosphorus-diffused silicon solar cell emitters passivated with plasma enhanced chemical vapor deposited silicon nitride and thermal silicon oxide, J. Appl. Phys. 89 (2001) 3821–3826, https://doi.org/10.1063/1.1350633.

[67] S. Duttagupta, F. Ma, B. Hoex, T. Mueller, A.G. Aberle, Optimised antireflection coatings using silicon nitride on textured silicon surfaces based on measurements and multidimensional modelling, Energy Procedia 15 (2012) 78–83, https://doi.org/10.1016/j.egypro.2012.02.009.

[68] Y. Wan, D. Yan, A. Cuevas, K.R. McIntosh. Influence of the $NH_3$:$SiH_4$ ratio and surface morphology on the surface passivation of phosphorus-diffused c-Si by PECVD $SiN_x$, IEEE, 2014, pp. 3317–3321. https://doi.org/10.1109/PVSC.2014.6925644.

[69] A. Kimmerle, M. Momtazur Rahman, S. Werner, S. Mack, A. Wolf, A. Richter, H. Haug, Precise parameterization of the recombination velocity at passivated phosphorus doped surfaces, J. Appl. Phys. 119 (2016), 025706, https://doi.org/10.1063/1.4939960.

[70] T.C. Kho, K.C. Fong, M. Stocks, K. McIntosh, E. Franklin, S.P. Phang, W. Liang, A. Blakers, Excellent ONO passivation on phosphorus and boron diffusion demonstrating a 25% efficient IBC solar cell, Prog. Photovoltaics Res. Appl. 28 (2020) 1034–1044, https://doi.org/10.1002/pip.3310.

[71] J. Melskens, R.J. Theeuwes, L.E. Black, W.J.H. Berghuis, B. Macco, P.C. P. Bronsveld, W.M.M. Kessels, Excellent passivation of n-type silicon surfaces enabled by pulsed-flow plasma-enhanced chemical vapor deposition of phosphorus oxide capped by aluminum oxide, Phys. Status Solidi Rapid Res. Lett. 15 (2021) 2000399, https://doi.org/10.1002/pssr.202000399.

[72] J.P. Niemelä, B. Macco, L. Barraud, A. Descoeudres, N. Badel, M. Despeisse, G. Christmann, S. Nicolay, C. Ballif, W.M.M. Kessels, M. Creatore, Rear-emitter silicon heterojunction solar cells with atomic layer deposited ZnO:Al serving as an alternative transparent conducting oxide to $In_2O_3$:Sn, Sol. Energy Mater. Sol. Cells 200 (2019) 109953, https://doi.org/10.1016/j.solmat.2019.109953.

[73] T.F. Wietler, B. Min, S. Reiter, Y. Larionova, R. Reineke-Koch, F. Heinemeyer, R. Brendel, A. Feldhoff, J. Krugener, D. Tetzlaff, R. Peibst, High temperature annealing of ZnO:Al on passivating POLO junctions: impact on transparency, conductivity, junction passivation, and interface stability, IEEE J. Photovoltaics. 9 (2019) 89–96, https://doi.org/10.1109/JPHOTOV.2018.2878337.

[74] B.W.H. Van De Loo, B. Macco, J. Melskens, W. Beyer, W.M.M. Kessels, Silicon surface passivation by transparent conductive zinc oxide, J. Appl. Phys. 125 (2019), https://doi.org/10.1063/1.5054166.

[75] Y. Wu, P.M. Hermkens, B.W.H. van de Loo, H.C.M. Knoops, S.E. Potts, M. A. Verheijen, F. Roozeboom, W.M.M. Kessels, Electrical transport and Al doping efficiency in nanoscale ZnO films prepared by atomic layer deposition, J. Appl. Phys. 114 (2013), 024308, https://doi.org/10.1063/1.4813136.

[76] D. Garcia-Alonso, S.E. Potts, C.A.A. van Helvoirt, M.A. Verheijen, W.M.M. Kessels, Atomic layer deposition of B-doped ZnO using triisopropyl borate as the boron precursor and comparison with Al-doped ZnO, J. Mater. Chem. C. 3 (2015) 3095–3107, https://doi.org/10.1039/C4TC02707H.

[77] D. Tetzlaff, J. Krügener, Y. Larionova, S. Reiter, M. Turcu, F. Haase, R. Brendel, R. Peibst, U. Höhne, J.D. Kähler, T.F. Wietler, A simple method for pinhole detection in carrier selective POLO-junctions for high efficiency silicon solar cells, Sol. Energy Mater. Sol. Cells 173 (2017) 106–110, https://doi.org/10.1016/j.solmat.2017.05.041.

[78] T.F. Wietler, D. Tetzlaff, J. Krügener, M. Rienäcker, F. Haase, Y. Larionova, R. Brendel, R. Peibst, Pinhole density and contact resistivity of carrier selective junctions with polycrystalline silicon on oxide, Appl. Phys. Lett. 110 (2017), https://doi.org/10.1063/1.4986924.

[79] H. Watanabe, N. Yamada, M. Okaji, Linear thermal expansion coefficient of silicon from 293 to 1000 K, Int. J. Thermophys. 25 (2004) 221–236, https://doi.org/10.1023/B:IJOT.0000022336.83719.43.

[80] H. Ibach, Thermal expansion of silicon and zinc oxide (II), Phys. Status Solidi 33 (1969) 257–265, https://doi.org/10.1002/pssb.19690330124.

[81] L. Hennen, E.H.A. Granneman, W.M.M. Kessels. Analysis of blister formation in spatial ALD $Al_2O_3$ for silicon surface passivation, IEEE, 2012, pp. 001049–001054. https://doi.org/10.1109/PVSC.2012.6317783.

[82] M. Zhao, Z.-T. Sun, W.-Y. Wu, C.-H. Hsu, X.-Y. Zhang, S.-Y. Lien, W.-Z. Zhu, Variation of oxygen vacancy defects in sALD-ZnO films annealed in an oxygen-rich ambient, ECS J. Solid State Sci. Technol. (2021), https://doi.org/10.1149/2162-8777/abd881.

[83] L. Tutsch, H. Sai, T. Matsui, M. Bivour, M. Hermle, T. Koida, The sputter deposition of broadband transparent and highly conductive cerium and hydrogen co-doped indium oxide and its transfer to silicon heterojunction solar cells, Prog. Photovoltaics Res. Appl. (2021) 3388, https://doi.org/10.1002/pip.3388.

[84] T. Pisarkiewicz, K. Zakrzewska, E. Leja, Scattering of charge carriers in transparent and conducting thin oxide films with a non-parabolic conduction band, Thin Solid Films 174 (1989) 217–223. http://www.sciencedirect.com/science/article/pii/0040609089908924.

[85] Y. Wu, A.D. Giddings, M.A. Verheijen, B. Macco, T.J. Prosa, D.J. Larson, F. Roozeboom, W.M.M. Kessels, Dopant distribution in atomic layer deposited ZnO: Al films visualized by transmission electron microscopy and atom probe tomography, Chem. Mater. 30 (2018), https://doi.org/10.1021/acs.chemmater.7b03501.

[86] D. Gaspar, L. Pereira, K. Gehrke, B. Galler, E. Fortunato, R. Martins, High mobility hydrogenated zinc oxide thin films, Sol. Energy Mater. Sol. Cells 163 (2017) 255–262, https://doi.org/10.1016/j.solmat.2017.01.030.

[87] M.V. Ponomarev, K. Sharma, M.A. Verheijen, M.C.M. van de Sanden, M. Creatore, Improved conductivity of aluminum-doped ZnO: the effect of hydrogen diffusion from a hydrogenated amorphous silicon capping layer, J. Appl. Phys. 111 (2012), 063715, https://doi.org/10.1063/1.3692439.
[88] C.H. Seager, D.S. Ginley, Passivation of grain boundaries in polycrystalline silicon, Appl. Phys. Lett. 34 (1979) 337–340, https://doi.org/10.1063/1.90779.
[89] T. Koida, H. Sai, M. Kondo, $In_2O_3$:H transparent conductive oxide films with high mobility and near infrared transparency for optoelectronic applications, Energy Mater. Mater. Sci. Eng. Energy Syst. 7 (2012) 102–107. http://www.scopus.com/inward/record.url?eid=2-s2.0-84876802257&partnerID=tZOtx3y1.
[90] S.C. Baker-Finch, K.R. McIntosh, Reflection of normally incident light from silicon solar cells with pyramidal texture, Prog. Photovoltaics Res. Appl. 19 (2011) 406–416, https://doi.org/10.1002/pip.1050.
[91] Z.C. Holman, M. Filipič, A. Descoeudres, S. De Wolf, F. Smole, M. Topič, C. Ballif, Infrared light management in high-efficiency silicon heterojunction and rear-passivated solar cells, J. Appl. Phys. 113 (2013), 013107, https://doi.org/10.1063/1.4772975.